Bulgarian Academy of Sciences. Space Research and Technology Institute.
Aerospace Research in Bulgaria. 38, 2026, Sofia

DOI: https://doi.org/10.3897/arb.v38.e13

SNOW MELT-OUT DATE IN THE TREELESS ZONE OF THE HIGHEST MOUNTAINS IN THE EASTERN BALKAN PENINSULA FROM SENTINEL-2 OBSERVATIONS

***Petar Dimitrov*[1], *Arthur Bayle*[2, 3]**

[1]*Space Research and Technology Institute – Bulgarian Academy of Sciences*
[2]*Climate Change Impacts and Risks in the Anthropocene (C-CIA),*
Institute for Environmental Sciences, University of Geneva
[3]*Department F.-A. Forel for Environmental and Aquatic Sciences, University of Geneva*
e-mail: petar.dimitrov@space.bas.bg

Keywords: *Alpine zone, Normalised difference snow index, Remote sensing, Satellite imagery*

Abstract

Measurements of Snow melt-out date (SMOD), the day of the year when seasonal snow disappears, from a limited number of climatological stations are unable to characterise the complex pattern of snow melting in mountain areas. Satellite remote sensing can help fill this knowledge gap. This study mapped the SMOD in the treeless zones of six mountainous regions in the eastern Balkans. Sentinel-2 Level-2A surface reflectance data in Google Earth Engine were used to implement a multiyear aggregation method, which previous studies have proven highly efficient with Landsat data. First, we analysed a set of Normalised Difference Snow Index (NDSI) images using Otsu's method to determine an optimal threshold to separate snow-free and snow-covered pixels. The optimal thresholds for the individual images varied, but were tightly clustered around the median value of 0.181. Then, we used this threshold and all Sentinel-2 data from 2017–2025 to estimate SMOD. The results were realistic in terms of both spatial and temporal patterns. We found that in the relatively low Osogovo Mountains, almost all snow cover (90%) disappeared by May 2, while in Pirin, this occurred on June 8. We also analysed the effect of the NDSI threshold on the SMOD estimates, showing that it is generally small in magnitude and spatially limited. The threshold of 0.40, often used in the literature, resulted in SMOD deviations of less than 10 days for 90% of pixels, compared with the optimal value of 0.181.

Introduction

Seasonal snow cover is a key characteristic of the climate of temperate mountains. In Bulgaria, situated in the eastern part of the Balkan peninsula, a persistent snow cover (i.e. a snow cover with continuous duration of over 30 days) is observed annually in mountainous areas at an altitude of over 1100–1400 m [1]. The number of days with snow cover increases with increasing elevation and reaches an average of 190–200 days per year on the highest peaks [1]. The Snow melt-out date (SMOD), i.e., the day of the year when the snow cover disappears, is one of the primary seasonal snow cover characteristics. The timing of snowmelt plays a significant role in ecosystem functioning. Later SMODs are usually associated with a delayed and potentially shorter growing season. Sites with prolonged snow cover are characterised by poorly developed soil and vegetation [2], lower plant diversity, and dominance of a few, well-adapted species [3, 4]. Studies in alpine and Arctic tundra environments [5, 6] indicate that flowering and other phenological events in some species are affected by snowmelt timing. Snow is also an important water reservoir that stores winter precipitation and contributes to runoff in spring and early summer [7]. Potential runoff production in these seasons is governed by the snowmelt timing and rate, among other factors [8]. However, despite the ecological, hydrological, and climatic importance [9–11] of snowmelt timing, spatially detailed information on SMOD is still lacking for the high mountains of Bulgaria and the eastern Balkan Peninsula. As a result, the strong local variability of snowmelt across alpine terrain remains poorly characterised in this region.

Different sources of information have been used to analyse temporal patterns in snowmelt at national to continental scales, including weather station measurements [10, 12, 13], spatial climatic datasets [11], and low-resolution satellite sensors [14–17]. However, these types of data are too coarse to provide an accurate spatial picture of snowmelt timing in the alpine zone of mountains where variations in SMOD of one or more weeks can be observed within just a few tens of meters. These irregularities are closely related to topography. Wind redistributes the snow, blowing it away from the ridge tops and exposed slopes and accumulating it in the protected bases of the slopes [18]. Gravitational snow transport processes, such as avalanches [19], lead to the removal of snow from higher elevation regions and deposition in regions of lower elevations. They are responsible for extreme snow depths at the base of steep slopes [20]. These processes contribute to snow depth variability and thus to the uneven melting across mountain terrain. The attempts to map snowmelt patterns at fine detail in mountain areas are relatively few and recent, although the Landsat satellites have allowed significant progress to be made in this area.

The practice of satellite remote sensing mapping of the extent of snow cover has a long history dating back to the first Landsat and Advanced Very High Resolution Radiometer (AVHRR) satellite missions [21]. While visual interpretation is usually considered the most accurate method to delineate snow-covered areas in a satellite image, automated approaches that minimise human intervention may be needed in some cases [22]. A common semi-automated approach is the one based on spectral indices. Such indices are designed to distinguish snow from other land cover types based on its spectral reflectance pattern. Pure snow cover is characterised by high reflectance in the visible and near-infrared part of the electromagnetic spectrum, followed by a sharp decrease toward the shortwave infrared part, where two well-expressed minimums at 1500 nm and 2000 nm are observed [23]. This is in contrast to vegetation and soil, which usually have much lower reflectance in the visible range [24] and to clouds, which have much higher reflectance in the shortwave infrared range [25]. Based on the Landsat Thematic Mapper (TM) bands, Dozier [21] suggested the normalised difference of Band 2 (520–600 nm) and Band 5 (1550–1750 nm), an index later known as Normalised Difference Snow Index (NDSI), as an indicator of the presence of snow. NDSI is now widely used, including for operational snow cover mapping [26].

The NDSI-based snow mapping approach relies on the selection of an appropriate threshold value. NDSI values greater than about 0.4 were found to represent snow cover well [21, 27]. However, it was recognised that an exact NDSI threshold for snow does not exist [22, 27, 28] and that the optimal threshold can vary within a certain range, depending on the image and the atmospheric corrections applied to the data. One can either find a credible value to apply to the analysis of several images [29] or select a threshold for each image [30–32], the choice depending on the specific task. The effect of the chosen threshold on SMOD mapping is a research topic that has received little attention to date.

While a single clear-sky image from platforms like Landsat and Sentinel-2 can be used to map snow cover over large areas with fine spatial resolution thanks to the NDSI, SMOD mapping remains challenging because it requires frequent observations. The number of clear sky observations depends on the revisit time of the satellite and the meteorological conditions, and it is generally insufficient to detect the SMOD on a yearly basis with those satellites. Recent studies have proposed utilising (aggregating) all observations within a period of several years, which enables a reliable estimation of the SMOD [29, 33, 34]. Such SMOD practically characterises the "average" snow-melting condition of the period. The method was tested with Landsat data for two 12-year periods by Bayle et al. [29] and Choler et al. [34]. However, further experimenting with this method, utilising the higher temporal and spatial resolution Sentinel-2 data and over other regions, is desirable.

To address the lack of fine-scale information on snowmelt timing in the high mountains of the eastern Balkans, this study applies a multiyear SMOD mapping approach to Sentinel-2 imagery for selected mountain regions in Bulgaria and adjacent areas. Building on the framework proposed by Bayle et al. [29] and Choler et al. [34], we aimed not only to map SMOD but also to determine an appropriate NDSI threshold for our study area and to assess the sensitivity of SMOD estimates to threshold choice and to the length of the aggregation period.

Study area

In this study we analyzed the SMOD in six mountainous regions from the eastern Balkan peninsula, including (Fig. 1): the western part of Stara planina Mountains at the border of Bulgaria and Serbia (SPW, 2168 m a.s.l.); the central part of Stara planina Mountains in Bulgaria (SPC, 2376 m a.s.l.); the Osogovo

Mountains at the border of Bulgaria and North Macedonia (OSO, 2251 m a.s.l.); the Vitosha Mountains in Bulgaria (VIT, 2290 m a.s.l.); the Pirin Mountains in Bulgaria including the Slavyanka/Orvilos mountain on the border with Greece (PSO, 2914 m a.s.l.); and Rila Mountains in Bulgaria (RIL, 2925 m a.s.l.). This study focuses on the high-altitude treeless zone characterised by alpine and subalpine grass and low shrub vegetation. The study area is formally defined as the area above 1600 m a.s.l., which is not covered by forest and dwarf mountain pine (*Pinus mugo* Turra) communities. The water bodies were also excluded.

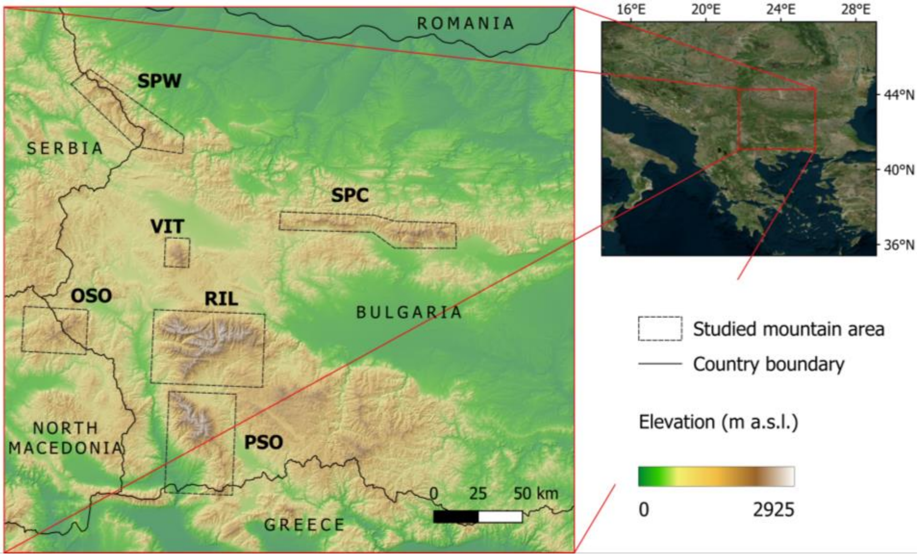

Fig. 1. Location of the six study areas in the eastern Balkan peninsula

Methods

SMOD mapping

A detailed description of the SMOD method used in this study can be found in Bayle et al. [29] and Choler et al. [34]. Here we briefly report the procedure, the data, and the settings used. All Sentinel-2 surface reflectance (Level 2A) images available in Google Earth Engine (GEE; [35]) between 2017 and 2025 (referred to as a data aggregation period) with less than 50% cloud cover which intersected the study areas were selected. Cloudy pixels were masked using the GEE Cloud Score+ dataset [36]. This dataset includes a quality assessment band (band “cs”) which grades the usability of individual pixels with respect to surface visibility on a continuous scale between 0 and 1, where 0 represents "not clear", while 1 represents "clear" observations. We masked out pixels with values of the “cs” band lower than 0.60. For each image, we calculated the NDSI using bands B3 and B11, namely NDSI = (B3 – B11) / (B3 + B11) and converted it to a binary image representing the snow extent where snow-covered pixels have value 1 and snow-free pixels have value 0. A pixel was labelled as snow-covered if its NDSI value was larger than a specified optimal threshold (see below). Each image was assigned the day of the year (DOY) corresponding to its acquisition date. Sorting the images by DOY enabled a densified annual time series to be obtained, where all acquisitions ranged between DOY 1 (January 1) and DOY 365 (December 31). The time series of binary images was smoothed using a centred moving median filter with a window size of 51 DOYs. It calculates, for each existing observation, the median of the observations which are within 25 DOYs from that observation. This procedure does not interpolate between observations but just smooths them. As a result, a time series of a "probability of snow" index [29], ranging between 0 and 1, was obtained. The observations before DOY 51 (February 20) were removed from the time series. The first observation in this shortened time series with a probability below 0.5 was identified as the SMOD. Pixels with "permanent snow", i.e. with probability always above 0.5, were assigned the value 365. Observations before DOY 51 were discarded to avoid detecting earlier DOYs due to snow onset after January 1 [29]. Finally, the SMOD image was masked to exclude forest/dwarf mountain pine, water, and areas below 1600 m. a.s.l. and exported from GEE at 20 m pixel size. We used Copernicus DEM to exclude low-altitude areas below 1600 m a.s.l. The water bodies were excluded using the European Space Agency's WorldCover 10 m 2021 product [37]. Finally, we used the CORINE Land Cover plus (CLCplus) Backbone 2023 [38] to exclude forest and dwarf mountain pine pixels. Forest was defined as the union of classes 2, 3, and 4. Dwarf mountain pine was excluded only in the study areas RIL and PSO, where it occupies a significant area. For that purpose, we excluded pixels belonging to the CLCplus Backbone class 5 (Low-growing woody plants). Note that in this way we excluded not only dwarf mountain pine communities but also areas covered by *Juniperus sibirica* or other shrubs that fall into this class. This was not the goal, so for the remaining study areas, where the risk of including dwarf mountain pine is minimal due to its limited distribution, we treated class 5 pixels as valid. For the SMOD mapping, we adapted the GEE script provided in Bayle et al. [29].

Optimal NDSI threshold

The optimal NDSI threshold for distinguishing between snow-covered and snow-free pixels in Sentinel-2 data was determined using the partially snow-covered images approach described in Bayle et al. [29]. Snow-covered surfaces are characterised by high NDSI values close to unity. In contrast, snow-free surfaces show lower, including negative, NDSI values. Therefore, when both types of surfaces appear on an image, the NDSI experiences a bimodal distribution. The thresholding method of Otsu [39] can be used to find a theoretical "optimal" threshold separating the two groups of pixels in the bimodal distribution of NDSI [22, 29, 40]. It is an unsupervised method of automatic threshold selection from a grey-level histogram [39]. We followed this approach by analysing Sentinel-2 surface reflectance images (Level 2A) for each study area. All images from April, May, June, and November with less than 5% cloud cover available in GEE were initially selected. Cloudy pixels were masked using the Cloud Score+ dataset as described in the previous section. Images from adjacent Sentinel-2 tiles having the same acquisition date were mosaicked. NDSI images were computed and masked to exclude forest/dwarf mountain pine, water, and areas below 1600 m a.s.l., as described above, and finally exported from GEE at 20 m pixel size. The terra package [41] in R [42] was used to generate a histogram of each image. The histograms were evaluated visually, and the images with bimodal histograms were selected. The R's package autothresholdr [43] was used to apply Otsu's threshold selection method on the selected images. We examined the difference in the thresholds between study areas using ANOVA and calculated the median of the thresholds to use as a generally applicable (for our study areas) "optimal" threshold.

SMOD dependence on the NDSI threshold and the length of the data aggregation period

The effect of the NDSI threshold and the length of the data aggregation period on the SMOD estimates was investigated for part of the RIL study area. To this aim, an image subset (1.6 km × 2.82 km, 11 280 pixels) was selected representing different geomorphologic features and slope expositions as well as a wide range of SMODs. The SMOD was calculated using thresholds from 0.0 to 0.4 in increments of 0.05, and the estimates were compared with those obtained by utilising the optimal threshold. Furthermore, we calculated SMOD for progressively shorter periods (excluding one year from the start of the initial nine-year period 2017–2025) to visually assess the effect of the reduction in the number of clear-sky observations on the quality of the SMOD map.

Results

A total of 414 NDSI images were exported from GEE for the six study areas. Most of them were not suitable for applying Otsu's method because one of the two pixel types, snow-covered or snow-free, dominated the scene, or because no valid pixels remained after applying the masks. A relatively balanced distribution of snow-covered and snow-free pixels was observed in the histograms of 67 of the images. These histograms showed a clear bimodal distribution, and the corresponding images were selected for further analysis. The number of suitable images varied depending on the size of the study area. Only 5 images were available for the smallest study area (VIT, Fig. 1), while 17 images could be used for PSO. The optimal threshold differences between study areas (Fig. 2a) were relatively small and not statistically significant according to the one-way ANOVA ($F(5, 61) = 0.942$, $p = 0.46$). The small sample size precludes further investigation of the possible specificity of the optimal threshold depending on the area studied. However, Fig. 2a suggests that the variation within a single study area surpasses the difference between study areas. The distribution of the optimal threshold for all study areas is shown in Fig. 2b. It shows a bimodal pattern with two closely located modes (~0.125 and ~0.195). Nevertheless, we decided to use a single optimal threshold determined as the median of the distribution, as this approach is objective and reproducible. The median optimal NDSI threshold was 0.181.

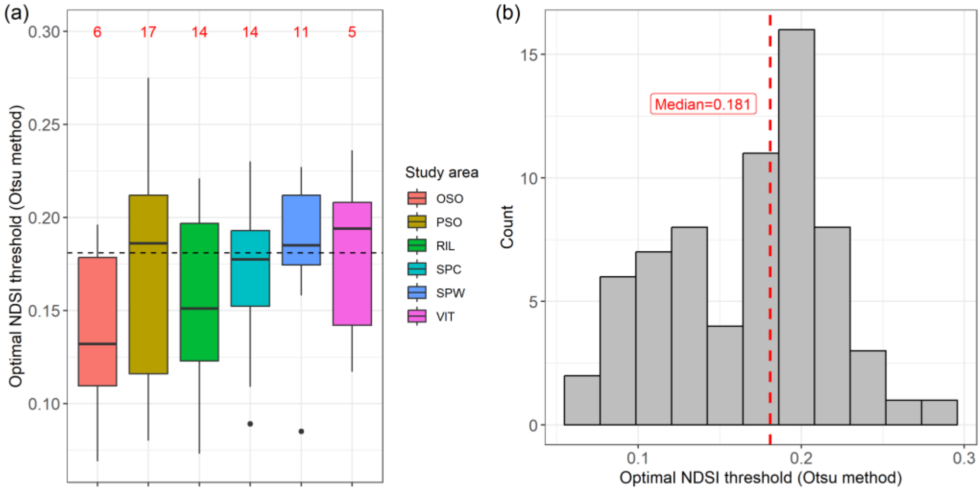

Fig. 2. Results of the optimal NDSI threshold analysis. (a) Boxplots of the optimal NDSI threshold for the study areas (Center line, median; box, interquartile range; upper/lower whisker, the largest/smallest value no further than 1.5× interquartile range from the box; dots, outliers). For the location of the study areas, see Figure 1. The red numbers at the top represent the sample size. (b) Distribution of the optimal NDSI threshold for all study areas. The median optimal NDSI threshold for all study areas is indicated by the horizontal line in (a) and the vertical line in (b).

Fig. 3 illustrates the estimated SMOD in the six study areas. The maps show credible patterns both within individual study areas and between them. The highest mountains, Rila and Pirin (study areas RIL and PSO, respectively), have later SMODs than the other study areas. A tendency for SMOD to increase with elevation is observed in each individual mountain area. The effect of exposition is clearly presented. For instance, the small subset image in Fig. 3f shows a ridge with an east-west direction in the Rila Mountains. The northerly exposed slopes, the upper half of the image, have later SMOD than those with south exposition, the bottom half of the image. The area marked with the red rectangle shows side ridges to the south of the main ridge with alternating late and early SMODs corresponding to slopes with northwest and southeast exposition, respectively. Finer patterns are also observed, such as localised late SMODs at the base of cirque walls in Rila and Pirin, and earlier SMODs at the wind-exposed ridge tops (as shown by the red ellipse in the subset in Fig. 3f) and on steep slopes with rock outcrops. Fig. 4 shows the cumulative distribution of pixels in each study area with respect to the SMOD. It can be used to find what percent of the pixels (respectively the area) has an earlier or later SMOD than a certain DOY. For instance, in SPC, about 40% of pixels have SMOD of DOY 100 (April 10) or earlier and in PSO, about 20% of pixels have SMOD later than DOY 150 (May 30). At PSO, the latest estimated SMOD is DOY 269 (September 26), and 90% of the pixels have SMOD not later than DOY 159 (June 8). At RIL, SPC, VIT, OSO, and SPW these figures are, respectively, DOY 234 (August 22) and DOY 146 (May 26), DOY 204 (July 23) and DOY 128 (May 8), DOY 179 (June 28) and DOY 133 (May 13), DOY 162 (June 11) and DOY 122 (May 2), DOY 159 (June 8) and DOY 126 (May 6). The SMOD algorithm identified 24 pixels (0.96 ha) in PSO as "permanent snow" (value 365 in Fig. 3). These were concentrated in the Golemia Kazan cirque (the subset image in Fig. 3e), Banski suhodol cirque, and Bayuvi dupki cirque. Two glacierets (1.68 ha) and several sustainable snow patches are indeed formed under present-day climatic conditions in Golemia Kazan and Banski suhodol, but not in Bayuvi dupki cirque [44, 45]. Fig. 4 also shows differences in the dynamics of snowmelt between study areas. In the lower mountains (OSO, SPC, and SPW), snowmelt starts rapidly and early, around mid-March (~DOY 75) and takes place at a constant rate. For the highest mountains (PSO and RIL), snow-melt in the beginning of spring is slower and accelerates in May (approximately after DOY 125, May 5).

The effect of the NDSI threshold on the SMOD estimates in the selected part of the RIL study area is shown in Fig. 5. The usage of thresholds lower than 0.181 resulted in later SMOD estimates, therefore positive difference (e.g. Fig. 5c) and the opposite, the thresholds larger than 0.181, which are stricter with respect to the snow-covered area detection, resulted in earlier SMOD estimates, thus, negative differences (e.g. Fig. 5d). The maximal differences exceeded 30 days but such deviations were more of an exception even with the extreme thresholds of 0.0 and 0.4. Using the 0.4 threshold, about 35% of the pixels had the same SMOD and another 40% had one to five days earlier SMOD compared to the optimal threshold (Fig. 5f). For thresholds between 0.10 and 0.25 the pixels with deviation of 10 or more days were about one percent and their share reached about 10% for threshold of 0.40 (Fig. 5g). In general, the differences are greatest in regions where SMOD change rapidly over short distance. In areas which are more homogeneous in terms of SMOD, the effect of the threshold is smaller.

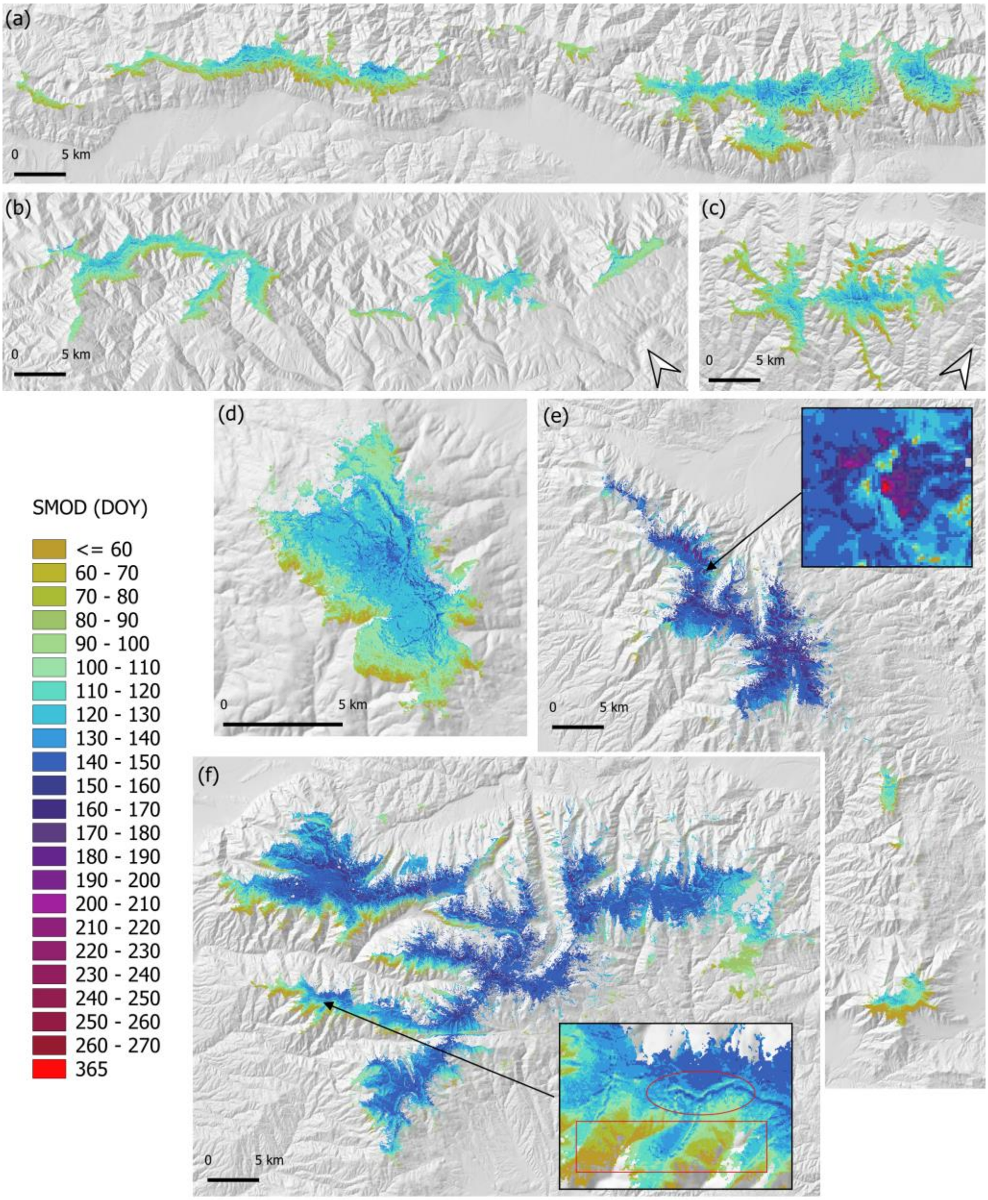

Fig. 3. SMOD in the six study areas estimated using Sentinel-2 observations from 2017 to 2025. (a) SPC, (b) SPW, (c) OSO, (d) VIT, (e) PSO, and (f) RIL. See the text for explanations of the image subsets in (e) and (f).

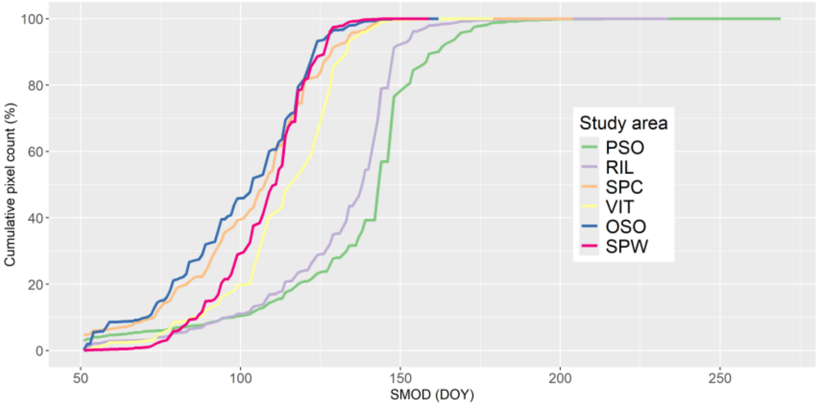

Fig. 4. Cumulative distribution of the SMOD estimates for the six study areas

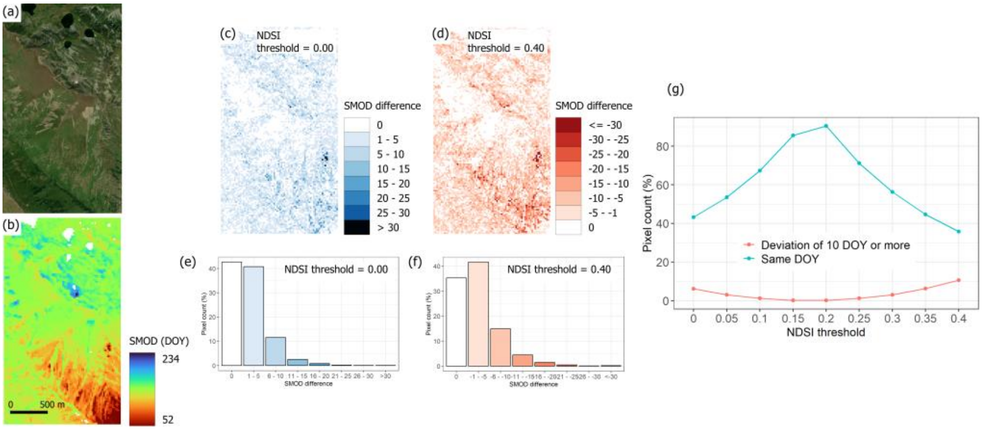

Fig. 5. Effect of the optimal NDSI threshold on the estimated SMOD in part of the RIL study area. (a) Satellite image (Microsoft Bing) of the analysed area. (b) SMOD was estimated using the optimal NDSI threshold from this study (0.181). (c) and (d) Difference in SMOD estimated using thresholds 0.0 and 0.4, respectively, and the SMOD estimated using the optimal threshold (calculated as SMOD0.0 minus SMOD0.181 and SMOD0.4 minus SMOD0.181, respectively). (e) and (f) Percentage distribution of the pixels among SMOD difference classes in images (c) and (d), respectively. (g) Percent of the pixels with no change in the estimated SMOD and with deviation of 10 days or more compared to the optimal threshold (0.181) for different NDSI thresholds.

The results from the experiment with different lengths of the aggregation period are shown in Fig. 6. The map created with one year of data failed to depict fine-scale patterns in the SMOD. The estimated SMOD was unstable in maps based on one to four years, and stabilised at five or more years. Little difference was observed between maps created with five and nine years of data.

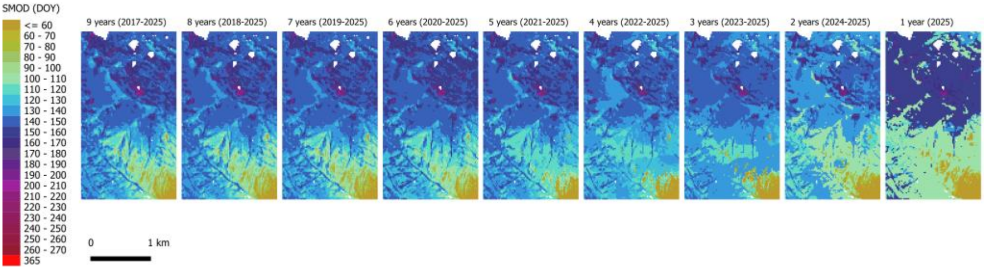

Fig. 6. SMOD estimated using Sentinel-2 data collected for periods of one to nine years in part of the RIL study area

Discussion

In this study, we presented the first detailed remote sensing-based maps of snowmelt timing for high-mountain areas in Bulgaria and adjacent regions. Only two climatological stations in the studied mountains, Cherni Vrah (Vitosha Mountain) and Vrah Botev (Stara Planina Mountains), are currently collecting snow depth data from which snowmelt date can be determined (https://hydro.bg/). Therefore, the presented approach can contribute significantly to spatial characterization and monitoring of snow cover melting pattens in this region.

Furthermore, we investigated the possibility of identifying an optimal NDSI threshold for Sentinel-2 data in this region. To this end, a statistical method based on the image histogram [39] was used, which has been shown by Yin et al. [22] to yield results very similar to those of an expert-derived threshold. Since the threshold value determined using Otsu's method [39] depends on the NDSI frequency distribution in the analysed image, which is determined by the land cover (e.g. vegetation and rock types [40]) and the proportion of the image covered by snow, it is necessary to analyse a large number of images. Studies by Bayle et al. [29] and Härer et al. [40] show that despite some variation, Otsu thresholds are highly concentrated around a certain value, and the mean (or median) can be used as a reasonable approximation. Using 67 images, we obtained a median threshold (0.181), which was very close to that of Bayle et al. [29], who analysed 121 Landsat images over the Pyrenees, the European Alps and the Greater Caucasus covering the period 1984–2023, and found the average optimal NDSI threshold to be 0.1543. Furthermore, both our study and that of Bayle et al. [29] used atmospherically corrected data, suggesting that compatible results can be obtained between Landsat and Sentinel-2 on the same processing level. Our optimal threshold is also close to the value of 0.2 used by Dimitrov [46] for a study area in the Rila Mountains and Landsat data. The results also comply with Poussin et al. [28], who found that the standard value of 0.4 underestimated the snow cover extent in their study area. On the other hand, Härer et al. [40] analysed Landsat images between 2010 and 2015 and found that, for two study areas in the European

Alps, the thresholds predicted by Otsu's method were clustered around 0.4. It is noteworthy that the data used in their study had a different processing level–top-of-atmosphere reflectance. Stoyanov [30, 31] determined the NDSI threshold for Sentinel-2 based on visual interpretation and also found it to be higher than our study – between 0.21 and 0.58 for the central part of the Stara Planina and between 0.34 and 0.69 for the Pirin Mountains. This may be due to different processing of the images [30, 31]. While the optimal threshold value determined in this study may not be perfect for each image, it is a convenient choice in scenarios when a large number of images are to be analysed, and a dynamic threshold selection method is not available or feasible.

Compared to the widely used value of 0.4 in the literature, our optimal threshold of 0.181 resulted in later SMOD estimates (Fig. 5). We do not have validation data to assess the accuracy of the two thresholds. However, for a small test area, we evaluated the relative effect of changing the threshold on SMOD and found that when our optimal threshold was used instead of the standard value of 0.4, only 10% of the pixels had SMOD that was 10 days or more later. Such small differences are supported by Fig. 7 illustrating that the snow cover extent determined using the two thresholds is very similar. The threshold of 0.181 includes more pixels that can be interpreted as "intermediate" between "typical" snow-covered and snow-free pixels on the false-colour composite image. Such "intermediate" pixels may have patchy and/or thin snow cover, occupying a different proportion of the pixel [28]. We conclude that Bayle et al.'s SMOD estimation method [29] is not very sensitive to the NDSI threshold used and provides reliable results with a range of values.

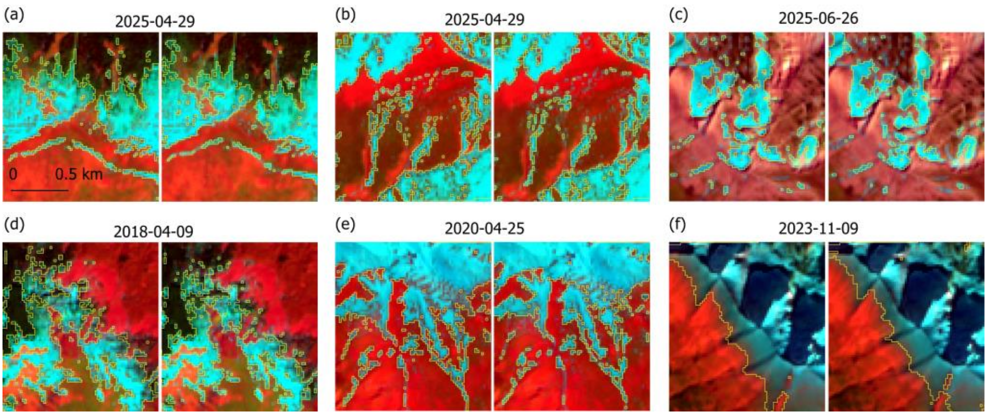

Fig. 7. Illustration of snow cover extent detected using two NDSI thresholds. Six image subsets, (a) to (f), are presented where the boundary (yellow line) superimposed on the left image is for a threshold of 0.181, and that on the right image is for a threshold of 0.4. Background images, false-colour composite images from Sentinel-2 (B11/B8A/B3). The date of the image is indicated for each subplot.

Bayle et al. [29] assessed the impact of the number of available Landsat clear-sky observations on SMOD estimates with their method and found that at least 15 observations were required for accurate results. Reducing the number of observations below 15 led to a rapid deterioration in the quality of the estimate. Therefore, a sufficiently long aggregation period is needed to ensure that an adequate number of observations are available for the entire or at least most of the area. This study used 9 years of Sentinel-2 data. Due to the high revisit frequency (5 days with two satellites, two to three days in the overlap areas of the swaths; [47]), Sentinel-2 satellites provide more cloud-free observations than Landsat satellites. Fig. 8 shows the number of clear-sky observations between March 1 and August 31 in the RIL study area for one year (2025) and for the entire period (2017–2025). The number of clear-sky observations for 2025 was between 10 and 20 for most of the area, and this was not enough for an accurate SMOD estimate, as seen from Fig. 6. For the period 2017–2025, clear-sky observations were between 80 and 130. In the eastern part of the study area, where there is an overlap of the swaths, the number of observations is approximately double. The ability to obtain good SMOD estimates with only five years, as suggested by Fig. 6, has important implications for the studies of SMOD change. However, our analysis was performed over a small area, and future change studies should determine the length of the aggregation period that is appropriate for their study area, as cloud frequency may differ.

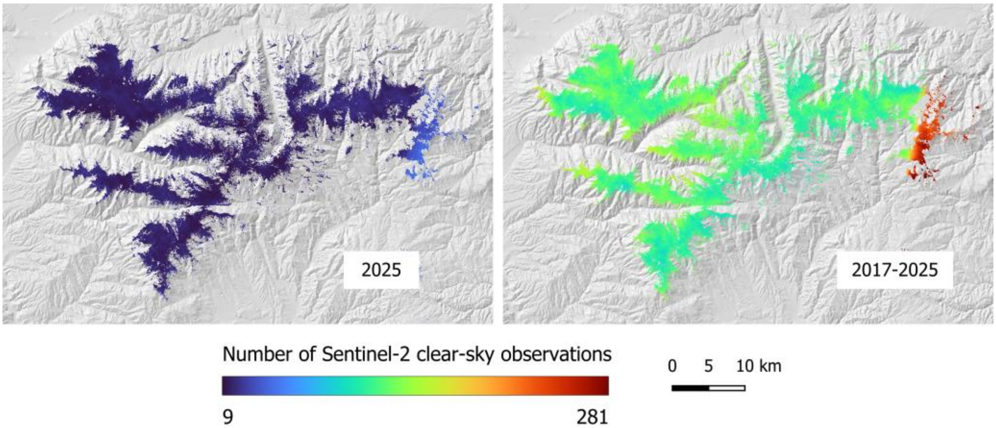

Fig. 8. Number of clear-sky observations in the RIL study area. The number of clear-sky observations between March 1 and August 31 are shown for 2025 (left-hand map) and for the entire period 2017–2025 (right-hand map).

Conclusion

This study created SMOD raster layers at 20 m resolution across six high-mountain areas in the eastern Balkan Peninsula following the methods in Bayle et al. [29] and Choler et al. [34], which represent the first fine-scale, spatially explicit snowmelt timing dataset in this region. The estimated SMODs showed credible spatial patterns related to altitude, exposition and topography. Melting of seasonal snow cover in the lower study areas, Osogovo Mountains and Stara Planina Mountains, occurs in the second half of March and in April. In these mountains, 90% of the open areas above 1600 m a.s.l are snow-free in early May. In the two highest surveyed areas, Pirin and Rila, this occurs in late May and early June. Vitosha Mountains occupy an intermediate position with respect to SMOD. Further studies should focus on validation of these results with data from climatological stations or other methods such as phenocameras. In addition, we determined an optimal NDSI threshold for 67 Sentinel-2 Level 2A images between 2017 and 2025 using Otsu's histogram method. The median optimal threshold value of 0.181 was close to a threshold reported in the literature for other temperate mountains and Landsat data [29]. An experiment carried out in part of one of the study areas showed that the effect of the NDSI threshold value on the SMOD estimates is relatively small and mostly expressed as isolated pixels in areas experiencing a large difference in SMOD over a small distance. Using the typical threshold of 0.40 resulted in only 10% of pixels having SMOD estimates deviating by 10 days or more, compared with the optimal value of 0.181. Our SMOD estimates were based on the full length of the Sentinel-2 L2A dataset available in GEE, i.e. nine years. However, a shorter aggregation period may be sufficient for a reliable estimate of SMOD, as suggested by the analysis of the number of available cloud-free Sentinel-2 observations and the "stabilisation" of the mapped SMOD pattern from five years onwards. The generated raster layers of SMOD, which are freely available on Zenodo [48], may find different applications, including in the distribution modelling of alpine plant species and communities and in hydrological studies.

References

1. Mateeva, Z. Precipitation and snow cover. In: Kopralev, I. (Ed) Geography of Bulgaria. Sofia, ForCom, 2002, 152–154. (In Bulgarian)
2. Choler, P., N. Bonfanti, A. Reverdy et al. Legacy of snow cover on alpine landscapes. Communications Earth and Environment, 2025, 6, 758. DOI: https://doi.org/10.1038/s43247-025-02702-6
3. Billings, W.D., L.C. Bliss. An Alpine Snowbank Environment and Its Effects on Vegetation, Plant Development, and Productivity. Ecology, 1959, 40 (3), 388–397.
4. Palaj, A., J. Kollár, N. Antalová. Impact of snow avalanches on alpine plant communities in the Tatra Mts. Biodiversity, 2025, 26(2), 174–180. DOI: https://doi.org/10.1080/14888386.2025.2460188

5. Vorkauf, M., A. Kahmen, C. Körner, E. Hiltbrunner. Flowering phenology in alpine grassland strongly responds to shifts in snowmelt but weakly to summer drought. Alpine Botany, 2021, 131, 73–88.
DOI: https://doi.org/10.1007/s00035-021-00252-z
6. Frei, E.R., G. H. R. Henry. Long-term effects of snowmelt timing and climate warming on phenology, growth, and reproductive effort of Arctic tundra plant species. Arctic Science, 2022, 8 (3), 700–721. DOI: https://doi.org/10.1139/as-2021-0028
7. Stewart, I.T. Changes in snowpack and snowmelt runoff for key mountain regions. Hydrol. Process., 2009, 23, 78–94. DOI: https://doi.org/10.1002/hyp.7128
8. Barnhart, T.B., C.L. Tague, N.P. Molotch. The counteracting effects of snowmelt rate and timing on runoff. Water Resources Research, 2020, 56, e2019WR026634. DOI: https://doi.org/10.1029/2019WR026634
9. Stone, R.S., E.G. Dutton, J.M. Harris, D. Longenecker. Earlier spring snowmelt in northern Alaska as an indicator of climate change. J. Geophys. Res. Atmos., 2002, 107, ACL 10-11–ACL 10-13.
10. Vorkauf, M., C. Marty, A. Kahmen, E. Hiltbrunner. Past and future snowmelt trends in the Swiss Alps: the role of temperature and snowpack. Climatic Change, 2021, 165, 44. DOI: https://doi.org/10.1007/s10584-021-03027-x
11. Akyurek, Z., S. Kuter, Ç.H. Karaman, B. Akpınar. Understanding the Snow Cover Climatology over Turkey from ERA5-Land Reanalysis Data and MODIS Snow Cover Frequency Product. Geosciences, 2023, 13, 311.
DOI: https://doi.org/10.3390/geosciences13100311
12. Ye, H. Increases in snow season length due to earlier first snow and later last snow dates over north central and northwest Asia during 1937–94. Geophysical research letters, 2001, 28 (3), 551–554. DOI: https://doi.org/10.1029/2000GL012036
13. Peng, S., S. Piao, P. Ciais et al. Change in snow phenology and its potential feedback to temperature in the Northern Hemisphere over the last three decades. Environ. Res. Lett., 2013, 8, 014008. DOI: https://doi.org/10.1088/1748-9326/8/1/014008
14. Rinne, J., M. Aurela, T. A. Manninen. Simple Method to Determine the Timing of Snow Melt by Remote Sensing with Application to the CO2 Balances of Northern Mire and Heath Ecosystems. Remote Sens., 2009, 1 (4), 1097–1107.
DOI: https://doi.org/10.3390/rs1041097
15. Malnes, E., S. R. Karlsen, B. Johansen, J. W. Bjerke, H. Tømmervik. Snow season variability in a boreal-Arctic transition area monitored by MODIS data. Environ. Res. Lett., 2016, 11, 125005.
DOI: https://doi.org/10.1088/1748-9326/11/12/125005
16. Anttila, K., T. Manninen, E. Jääskeläinen, A. Riihelä, P. Lahtinen. The Role of Climate and Land Use in the Changes in Surface Albedo Prior to Snow Melt and the Timing of Melt Season of Seasonal Snow in Northern Land Areas of 40° N–80° N during 1982–2015. Remote Sens., 2018, 10, 1619.
DOI: https://doi.org/10.3390/rs10101619
17. Tomaszewska, M. A., G. M. Henebry. Changing snow seasonality in the highlands of Kyrgyzstan. Environ. Res. Lett., 2018, 13, 065006.
DOI: https://doi.org/10.1088/1748-9326/aabd6f

18. Mott, R., V. Vionnet, T. Grünewald. The Seasonal Snow Cover Dynamics: Review on Wind-Driven Coupling Processes. Frontiers in Earth Science, 2018, 6, 197. DOI: https://doi.org/10.3389/feart.2018.00197
19. Panayotov, M. Avalanches on the northwestern slope of peak Todorka (Pirin Mts, SW Bulgaria) and their influence on forests. Phytologia Balcanica, 2011, 17 (2), 237–246.
20. Bernhardt, M., K. Schulz. SnowSlide: A simple routine for calculating gravitational snow transport. Geophysical Research Letters, 2010, 37 (11), L11502. DOI: https://doi.org/10.1029/2010GL043086
21. Dozier, J. Spectral signature of alpine snow cover from the Landsat Thematic Mapper. Remote Sensing of Environment, 1989, 28, 9–22.
22. Yin, D., X. Cao, X. Chen, Y. Shao, J. Chen. Comparison of automatic thresholding methods for snow-cover mapping using Landsat TM imagery. International Journal of Remote Sensing, 2013, 34 (19), 6529–6538. DOI: https://doi.org/10.1080/01431161.2013.803631
23. Zhang, J. Z. Zhou. Spectra reflectance characteristics of different snow and snow-covered land surface objects and mixed spectrum fitting. In: 19th International Conference on Geoinformatics, Shanghai (China), 24–26 June 2011. IEEE, 1–4. DOI: https://doi.org/10.1109/GeoInformatics.2011.5980696
24. Dozier, J., R. O. Green, A. W. Nolin, T. H. Painter. Interpretation of snow properties from imaging spectrometry. Remote Sensing of Environment, 2009, 113, S25–S37. DOI: https://doi.org/doi:10.1016/j.rse.2007.07.029
25. Crane, R. G., M. R. Anderson. Satellite discrimination of snow/cloud surfaces. International Journal of Remote Sensing, 1984, 5 (1), 213–223.
26. Gascoin, S., M. Grizonnet, M. Bouchet, G. Salgues, O. Hagolle. (2019) Theia Snow collection: high-resolution operational snow cover maps from Sentinel-2 and Landsat-8 data. Earth System Science Data, 2019, 11, 493–514. DOI: https://doi.org/10.5194/essd-11-493-2019
27. Hall, D. K., G. A. Riggs, V. V. Salomonson. Development of Methods for Mapping Global Snow Cover Using Moderate Resolution Imaging Spectroradiometer Data. Remote Sensing of Environment, 1995, 54, 127–140.
28. Poussin, C., P. Timoner, B. Chatenoux, G. Giuliani, P. Peduzzi. Improved Landsat-based snow cover mapping accuracy using a spatiotemporal NDSI and generalized linear mixed model. Science of Remote Sensing, 2023, 7, 100078. DOI: https://doi.org/10.1016/j.srs.2023.100078
29. Bayle, A., S. Gascoin, C. Corona, M. Stoffel, P. Choler. Snow melt-out date (SMOD) change spanning four decades in European temperate mountains at 30 m from Landsat time series. Scientific Data, 2025, 12, 706. DOI: https://doi.org/10.1038/s41597-025-05044-2
30. Stoyanov, A. Application of Sentinel-2 satellite data for monitoring snow cover in territory of “Central Balkan”, Stara planina. In: Proceedings of the 20th Conference Space, Ecology, Safety – SES2024, Sofia (Bulgaria), 22–25 October 2024. SRTI-BAS, Sofia, 181–186. (In Bulgarian with English summary)
31. Stoyanov, A. Application of Sentinel-2 satellite data for monitoring snow cover in territory of Pirin Mountain for period of 10 years. In: Proceedings of the 21st Conference Space, Ecology, Safety – SES2025, Sofia (Bulgaria), 21–25 October 2025. SRTI-BAS, Sofia, 187–192. (In Bulgarian with English summary)

32. Anastasova, E., G. Kadinov, T. Djamiykov. Remote Sensing-Based Monitoring of Snow Cover Dynamics in Rila National Park. XXXIV International Scientific Conference Electronics (ET), Sozopol, Bulgaria, 2025, 1–4. DOI: https://doi.org/10.1109/ET66806.2025.11204053.
33. Panchard, T., O. Broennimann, M. Gravey, G. Mariethoz, A. Guisan. Snow cover persistence as a useful predictor of alpine plant distributions. Journal of Biogeography, 2023, 50, 1789–1802. DOI: https://doi.org/10.1111/jbi.14689
34. Choler, P., A. Bayle, N. Fort, S. Gascoin. Waning snowfields have transformed into hotspots of greening within the alpine zone. Nature Climate Change, 2025, 15, 80–85. DOI: https://doi.org/10.1038/s41558-024-02177-x
35. Gorelick, N., M. Hancher, M. Dixon et al. Google Earth engine: planetary-scale geospatial analysis for everyone. Remote Sensing of Environment, 2017, 202, 18–27. DOI: https://doi.org/10.1016/j.rse.2017.06.031
36. Pasquarella, V.J., C. F. Brown, W. Czerwinski, W. J. Rucklidge. Comprehensive Quality Assessment of Optical Satellite Imagery Using Weakly Supervised Video Learning. In: 2023 IEEE/CVF Conference on Computer Vision and Pattern Recognition, Vancouver (Canada), 17–24 June 2023. IEEE, 2125–2135. DOI: https://doi.org/10.1109/CVPRW59228.2023.00206
37. Zanaga, D., R. Van De Kerchove, D. Daems et al. ESA WorldCover 10 m 2021 v200. 2022. [Data set]. DOI: https://doi.org/10.5281/zenodo.7254221
38. European Environment Agency. CLCplus Backbone 2023 (raster 10 m), Europe, 2-yearly. 2025. [Data set]. DOI: https://doi.org/10.2909/b0bd43c6-1fa1-4d88-9c45-98b13a95d0b2
39. Otsu, N. A threshold selection method from gray-level histograms. IEEE Transactions on Systems, Man, and Cybernetics, 1979, 9 (1), 62–66. DOI: https://doi.org/10.1109/TSMC.1979.4310076
40. Härer, S., M. Bernhardt, M. Siebers, K. Schulz. On the need for a time- and location-dependent estimation of the NDSI threshold value for reducing existing uncertainties in snow cover maps at different scales. The Cryosphere, 2018, 12, 1629–1642. DOI: https://doi.org/10.5194/tc-12-1629-2018
41. Hijmans, R. J. terra: Spatial Data Analysis. R package version 1.7-23. 2023. URL: https://CRAN.R-project.org/package=terra
42. R Core Team. R: A language and environment for statistical computing. R Foundation for Statistical Computing, Vienna, Austria. 2021. URL: https://www.R-project.org/
43. Landini, G., D, Randell, S. Fouad, A. Galton. Automatic thresholding from the gradients of region boundaries. Journal of Microscopy, 2017, 265 (2), 185–195.
44. Gachev, E. M. Holocene glaciation in the mountains of Bulgaria. Mediterranean Geoscience reviews, 2020, 2, 103–117. DOI: https://doi.org/10.1007/s42990-020-00028-3.
45. Gachev, E. M. Response of Very Small Glaciers to Climate Variations and Change: Examples from the Pirin Mountains, Bulgaria. Atmosphere, 2022, 13, 859. DOI: https://doi.org/10.3390/atmos13060859
46. Dimitrov, I. Meteorological quantities for the snowmelt runoff model for Musalenska Bistritsa river basin. Annual of Sofia University "St. Kliment Ohridski", Faculty of Geology and Geography, Book 2 – Geography, 2022, 114, 169–185. (In Bulgarian with English summary)

47. Drusch, M., U. Del Bello, S. Carlier et al. Sentinel-2: ESA's Optical High-Resolution Mission for GMES Operational Services. Remote Sensing of Environment, 2012, 120, 25–36. DOI: https://doi.org/10.1016/j.rse.2011.11.026
48. Dimitrov, P., A. Bayle. Sentinel-2 derived snow melt-out date (SMOD) maps of six mountain areas in the eastern Balkan peninsula. 2026. [Data set]. DOI: https://doi.org/10.5281/zenodo.19093276

ДАТА НА СТОПЯВАНЕ НА СНЕЖНАТА ПОКРИВКА В БЕЗЛЕСНАТА ЗОНА НА НАЙ-ВИСОКИТЕ ПЛАНИНИ В ИЗТОЧНИТЕ БАЛКАНИ ПО НАБЛЮДЕНИЯ ОТ SENTINEL-2

П. Димитров, А. Бел

Резюме

Измерванията на снежната покривка в планинските райони обикновено се извършват в ограничен брой климатични станции, което не позволява да се оценят съществените пространствени различия в датата на стопяването и, които са характерни за тези райони. Спътниковите дистанционни наблюдения предоставят данни способни да запълнят тази празнина. Това проучване картографира датата на стопяване на снежната покривка (ДССП) във високопланинската безлесна зона на шест планински региона в източната част на Балканския полуостров използвайки данни от Sentinel-2 Level-2A и многогодишен метод за агрегиране, който е бил вече успешно тестван с данни от Landsat. Първоначално анализирахме хистограмите на набор от изображения на спектралния индекс Normalized Difference Snow Index (NDSI), използвайки метода на Otsu, за да определим оптимален праг за разделяне на пикселите със и без сняг. Оптималните прагове за отделните изображения варираха, но бяха добре концентрирани около медианата от 0,181. Тази прагова стойност беше впоследствие използвана за картографиране на ДССП на базата на всички данни от Sentinel-2 за периода 2017–2025 г. Получените карти представят реалистично както относителните пространствените различия, така и момента на стопяване на снежната покривка във времето. Оценките показват, че в относително ниската Осоговска планина почти цялата снежна покривка (90%) се стопява до 2 май, докато в Пирин това се става на 8 юни. Анализирахме също така ефекта на праговата стойност на NDSI върху оценките на ДССП, показвайки, че като цяло той е малък по величина и ограничен в пространството. Прагът от 0,40, често използван в литературата, доведе до отклонения на ДССП по-малки от 10 дни за 90% от пикселите, в сравнение с оптималната стойност от 0,181.